Collective excitations in three-dimensional Dirac systems

Collective excitations in three-dimensional Dirac systems

Q. N. Li,[1,2] P. Vasilopoulos,[3] F. M. Peeters,[2,4,5] W. Xu,[1,5,6,*] Y. M. Xiao,[1,†] and M. V. Milošević[2,‡]

[1]*School of Physics and Astronomy and Yunnan Key Laboratory of Quantum Information, Yunnan University, Kunming 650091, China*
[2]*Department of Physics, University of Antwerp, Groenenborgerlaan 171, B-2020 Antwerpen, Belgium*
[3]*Department of Physics, Concordia University, Montreal, Canada*
[4]*Departamento de Física, Universidade Federal do Ceará, 60455-760 Fortaleza, Ceará, Brazil*
[5]*Micro Optical Instruments Inc., Shenzhen 518118, China*
[6]*Key Laboratory of Materials Physics, Institute of Solid State Physics, HFIPS, Chinese Academy of Sciences, Hefei 230031, China*

(Dated: July 10, 2024)

We provide the plasmon spectrum and related properties of the three-dimensional (3D) Dirac semimetals (DSMs) Na_3Bi and Cd_3As_2 based on the random-phase approximation (RPA). The necessary one-electron eigenvalues and eigenfunctions are obtained from an effective $\mathbf{k}\cdot\mathbf{p}$ Hamiltonian. Below the energy at which the velocity v_z along the k_z axis vanishes, the density of states differs drastically from that of a 3D electron gas (3DEG) or graphene. The dispersion relation is anisotropic for wave vectors parallel (q) and perpendicular (q_z) to the (x,y) plane and is markedly different than that of graphene or a 3DEG. The same holds for the energy-loss function. Both depend sensitively on the position of the Fermi energy E_F relative to the region of the Berry curvature of the bands. For E_F below the energy at which v_z vanishes, the range of the relevant wave vectors q and q_z shrinks, for q_z by about one order of magnitude.

I. INTRODUCTION

In the last decade three-dimensional (3D) Dirac semimetals (DSMs), in which doubly degenerate conduction and valence bands cross linearly at one or more Dirac points, have been studied extensively [1–8]. The electronic dispersion relation of the low-energy excitations around the Dirac points is linear and resembles the massless Dirac equation of relativistic particle physics. In particular, it has been found that Na_3Bi and Cd_3As_2 are 3D DSMs that have two symmetry Dirac points connected by a pair of opposite chiral Fermi arcs [2, 3].

Angle-resolved photoemission spectroscopy (ARPES) experiments unveil a pair of stable 3D bulk Dirac points in both Na_3Bi and Cd_3As_2 located on opposite sides of the Brillouin zone center (Γ piont) which are protected by crystal symmetries [4–8]. The Fermi arc surface state, Berry curvatures, and anisotropic energy dispersions are observed as well in their 3D energy bands which is in line with theoretical predictions [4, 6]. This unique energy dispersion of 3D DSMs leads to many interesting properties, such as ultrahigh carrier mobilities [9–11], chiral anomalies [12, 13], topological phase transitions [14, 15], ultrafast transient times [16], nonlinear optical responses [19, 20], and quantum Hall effect in thin films [17] and in the bulk [18]. Reviews of their properties, as well as of those of Weyl semimetals, can be found in Refs. [21] and [22].

Despite the strong research activity in DSMs, we find that their collective excitations have not been studied as extensively as other properties. We are aware only of the studies of Ref. [23] for Na_3Bi and Cd_3As_2, of Refs. [24, 25] for general 3D DSMs, and of Ref. [26] for $PtTe_2$. In all of them only limited aspects of these excitations have been studied with very simplified energy spectra that are valid only very close to the Dirac points. In particular, Ref. [24] used the spectrum $E_{\mathbf{k},s} = s\hbar v_F\mathbf{k}$, where $\mathbf{k}$ is the 3D momentum, v_F is the Fermi velocity, and s the band index. This spectrum was criticized in Ref. [21]. Transport studies of 3D DSMs indicate that the simple energy spectra cannot explain their electronic excitations well due to their unique electronic band structures so that their plasmon modes remain unclear [10, 11].

The aim of this work is to present a comprehensive RPA treatment of collective excitations in Na_3Bi and Cd_3As_2 using the broadly accepted energy spectrum of the $\mathbf{k}\cdot\mathbf{p}$ approximation [2, 3], i.e., without unnecessary simplifications, and present a full account of the plasmon spectrum and of the corresponding energy loss. Using the energy band structures of 3D DSMs we found that their collective excitations are anisotropic and sensitively affected by the Berry curvature of the bands. This is in sharp contrast to graphene or other 3D systems like layered graphene [27], Weyl semimetals [28], and 3D DSMs with isotropic Dirac cones [26].

The work is organized as follows. In Sec. II, we present the basics of the one-electron aspects and in Sec. III the relevant dielectric functions. In Sec. IV, we present our results and discussion and in Sec. V our summary.

II. ONE-ELECTRON ASPECTS

Na_3Bi is a hexagonal crystal normally in its $P6_3/mmc$ or D^4_{6h} phase. There are two nonequivalent Na sites noted as Na(1) and Na(2). Na(1) and Bi can form simple honeycomb lattice layers stacked along the c-axis. The Na(2) atoms are sandwiched between the above-mentioned lattice layers and connect to the Bi atoms in forming the layers of honeycomb lattices. Na_3Bi has an inverted band structure and its Fermi surface consists of two isolated Fermi points [2]. Both time-reversal and inversion symmetries are present in Na_3Bi so that there is fourfold degeneracy at each Fermi point around which

* wenxu˙issp@aliyun.com
† yiming.xiao@ynu.edu.cn
‡ milorad.milosevic@uantwerpen.be

the band dispersion can be linearized. Due to the lattice structure, asymmetric features of the electronic band structure are expected for Na_3Bi Dirac fermions. In the $\mathbf{k}\cdot\mathbf{p}$ approximation [2], the Hamiltonian for low-energy electrons is given by

$$H(\mathbf{K}) = \varepsilon_{\mathbf{K}} \times I + \begin{pmatrix} M_{\mathbf{K}} & Ak_+ & 0 & B^*_{\mathbf{K}} \\ Ak_- & -M_{\mathbf{K}} & B^*_{\mathbf{K}} & 0 \\ 0 & B_{\mathbf{K}} & M_{\mathbf{K}} & -Ak_- \\ B_{\mathbf{K}} & 0 & -Ak_+ & -M_{\mathbf{K}} \end{pmatrix}, \quad (1)$$

where $\mathbf{K} = (\mathbf{k}, k_z) = (k_x, k_y, k_z)$ is the electron wave vector or momentum operator, and I is the 4×4 unitary matrix. The z-axis is the direction of stacking honeycomb lattice layers to form Na(1) and Bi. Further, $k_\pm = k_x \pm ik_y$, $\varepsilon_{\mathbf{K}} = C_0 + C_1k_z^2 + C_2k^2$, $M_{\mathbf{K}} = M_0 - M_1k_z^2 - M_2k^2$, and C_0, C_1, C_2, M_0, M_1, M_2 and A are band parameters [2, 29]. In Eq. (1), $B_{\mathbf{K}} = B_3k_zk_+^2 \sim K^3$ gives a high-order contribution to the electron motion, which is significant only at relatively large electron momentum. The corresponding Schrödinger equation can be solved analytically and the eigenvalues obtained are $E_\pm(\mathbf{K}) = \varepsilon_{\mathbf{K}} \pm [M_{\mathbf{K}}^2 + A^2k^2 + |B_{\mathbf{K}}|^2]^{1/2}$, where the $+$ $(-)$ sign refers to the conduction (valence) band. There exist two Dirac points at $k = 0$ and $k_z = \pm k_c = \pm[M_0/M_1]^{1/2}$, see Fig. 1.

The ARPES and spin-resolved ARPES measurements indicate that the energy bands for both Na_3Bi and Cd_3As_2 are spin degenerate near the Dirac points [4, 7] and the observable energy band splitting occurs in large energy and high magnetic field ranges [30]. These experimental works are in good agreement with theoretical predictions for Na_3Bi and Cd_3As_2 [2, 3]. The plasmons, induced by electron-electron (e-e) interactions mainly occur in low-energy and small-momentum regimes, in which case a spin degeneracy occurs. Thus, we can neglect the high-order terms containing $B_{\mathbf{K}}$ in Eq. (1). The 4×4 matrix becomes block-diagonal in form with two 2×2 matrices, the upper-left block $H_u(\mathbf{K})$ and lower-right block $H_l(\mathbf{K})$, respectively. By time reversal symmetry of 3D DSMs, we have $H_l(\mathbf{K}) = H_u^*(-\mathbf{K})$ [21]. This allows us to focus on studying the $H_u(\mathbf{K})$ which reads

$$H_u(\mathbf{K}) = \begin{pmatrix} \varepsilon_{\mathbf{K}} + M_{\mathbf{K}} & Ak_+ \\ Ak_- & \varepsilon_{\mathbf{K}} - M_{\mathbf{K}} \end{pmatrix}. \quad (2)$$

The resulting eigenvalues and eigenfunction of Eq. (2) are, respectively,

$$E_{\mathbf{K},l} = \varepsilon_{\mathbf{K}} + l\left[M_{\mathbf{K}}^2 + A^2k^2\right]^{1/2} = \varepsilon_{\mathbf{K}} + l\left[\xi_{\mathbf{K},l} + M_{\mathbf{K}}\right], \quad (3)$$

where $l = +1$ (-1) represents the conduction (valence) band, and

$$\psi_{\mathbf{K},l}(\mathbf{R}) = |\mathbf{K}, l\rangle = a_{\mathbf{K},l} \begin{pmatrix} 1 \\ b_{\mathbf{K},l} \end{pmatrix} e^{i\mathbf{K}\cdot\mathbf{R}}, \quad (4)$$

with $\mathbf{R} = (x, y, z)$, $\xi_{\mathbf{K},l} = \left[M_{\mathbf{K}}^2 + A^2k^2\right]^{1/2} - lM_{\mathbf{K}}$,

$$a_{\mathbf{K},l} = Ak(\xi_{\mathbf{K},l}^2 + A^2k^2)^{-1/2}, \qquad b_{\mathbf{K},\mathbf{l}} = l\xi_{\mathbf{K},l}/Ak_-. \quad (5)$$

Eqs. (1) - (5) also apply to Cd_3As_2 but with different parameters [29].

It's worth emphasizing that the band structures of 3D DSMs are different from those of single-layer or multilayer 3D DSMs. In the bulk 3D DSM samples that are unconfined along the z-axis, k_z is a continuous variable while in confined systems k_z is quantized for sufficiently small thicknesses due to the formed quantum-well structure [2, 3]. The finite-size effect removes the band inversion and opens a band gap for sufficiently thin samples [3, 31]. The effect weakens with increasing thickness and eventually the band inversion is restored. A recent experimental study confirmed this prediction in Cd_3As_2 thin films indicating that this feature is unique and worth exploring it further [15]. In our case the bulk 3D DSMs are extended and, in line with Eqs. (2) and (4), there is no finite-size effect to consider.

In Fig. 1 we show the energy dispersions $E_{\mathbf{K}}$ of Na_3Bi (left panels) and of Cd_3As_2 (right panels) given by Eq. (3). The first row of panels shows the full dispersions, the second one shows them as functions of k for fixed $k_z = k_c$, and the third as functions of k_z, for $k = 0$. We notice the following features.

(i) Both Na_3Bi and Cd_3As_2 have two symmetric Dirac points at the bottom of conduction band and at the top of the valence band for $k = 0$ and $k_z = \pm k_c$. The corresponding energies are $E_0 = C_0 + C_1M_0/M_1$ ($Na_3Bi \sim 7.62$ meV, $Cd_3As_2 \sim -218.68$ meV).

(ii) Near the two Dirac points the electron energies are approximately linear, but the dispersions for both bands are asymmetric and depend nonlinearly on k and k_z.

(iii) The dispersions along the k_z direction for both systems show arch-bridge-like Berry curvatures from $-k_c$ to k_c in both conduction and valence bands. The top of the arch-bridge-like energy spectrum is reached at $k = k_z = 0$, which is in contrast to a conventional 3D electron system where the minimum of the conduction band is at $k = 0$ and $k_z = 0$. The top of the Berry curvature in the conduction band is at $E_1 = C_0 + |M_0|$ ($Na_3Bi \sim 23$ meV, $Cd_3As_2 \sim -209$ meV).

(iv) The Berry curvatures in the energy bands imply that the electronic density of states (DOS) should be much smaller for $E < E_1$ than that for $E > E_1$ in n-doped 3D DSMs. Because the effect of Berry curvature in Na_3Bi is stronger than in Cd_3As_2, the DOS in Na_3Bi should also change more than in Cd_3As_2.

(v) The condition of carrier number conservation determines the Fermi energy E_F. With N_e the electron density and $f_+(E_{\mathbf{K},+}) = [e^{(x-E_F^+)/k_BT} + 1]^{-1}$ the Fermi-Dirac distribution for electrons reads

$$N_e = \frac{1}{\pi^2}\int_0^\infty dk_z \int_0^\infty dk k f_+(E_{\mathbf{K},+}). \quad (6)$$

For n-doped Na_3Bi, the Fermi level E_F is in the conduction band and the Fermi wave vector k_F along the k_z axis is much larger than along the k direction; near the Dirac points it's about 10-20 times larger. But for Cd_3As_2 k_F along the k direction, it is about twice larger than along the k_z axis. Accordingly, the electronic transitions will be different in Na_3Bi along the k or k_z directions, but in Cd_3As_2 these differences will be smaller. This conclusion, that Na_3Bi has stronger anisotropic properties than Cd_3As_2, has already been pointed out in the literature [2–6].

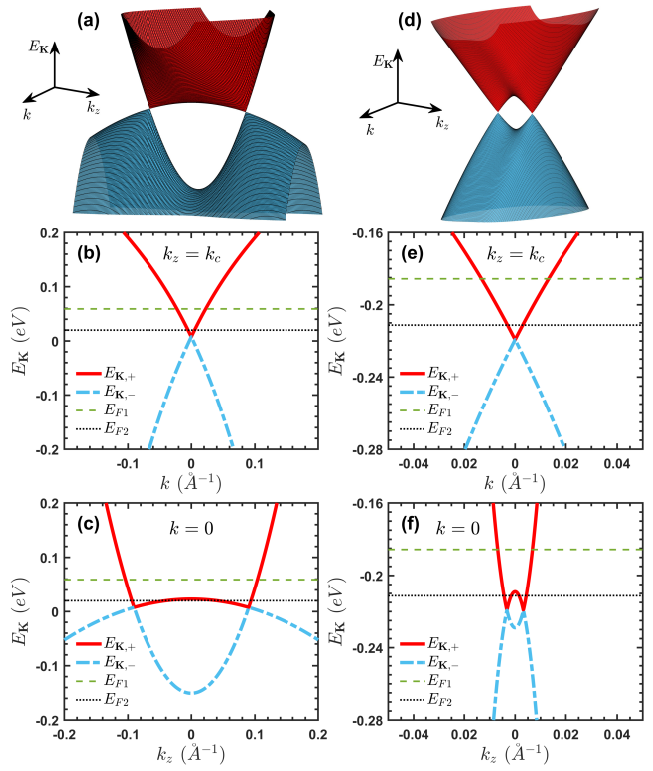

FIG. 1. (a) Energy dispersion $E_{\mathbf{K}}$ of Na_3Bi as a function of k and k_z, as given by Eq. (3). (b) $E_{\mathbf{K}}$ as a function of k at $k_z = k_c$. The Dirac point is at $k = 0$ with energy $E_0 = 7.6$ meV. (c) $E_{\mathbf{K}}$ as a function of k_z at $k = 0$. There are two Dirac points at $k_z = \pm k_c$. The top of the Berry curvature in the conduction band is $E_1 \simeq 23$ meV, its bottom in the valence band at $E_2 \simeq -151$ meV, and they are both located at $k = 0$ and $k_z = 0$. (d), (e), (f): *idem.* as in (a), (b), and (c), respectively, for Cd_3As_2. The energy of the Dirac point is at $E_0 \simeq -218.68$ meV. The top of the Berry curvature in the conduction band is $E_1 \simeq -209$ meV and its bottom in the valence band at $E_2 \simeq -229$ meV. The red curve shows the conduction band and the blue-dash-dotted curve is the valance band. The green-dashed and black-dotted lines show the Fermi energy E_F for high and low electron density, respectively, see Figs. 3 - 6.

(vi) It should be noted that the magnitude of the Fermi velocity $v_F = 2A$ in Na_3Bi ($\simeq 7.473 \times 10^5$ m/s) is similar to that in Cd_3As_2 ($\simeq 7.6 \times 10^5$ m/s). This is because the electron effective mass in Cd_3As_2 [32] ($\sim 0.02 - 0.042$ m$_e$), as found experimentally, is much smaller than that in Na_3Bi [10] ($\sim 0.11 - 0.24$ m$_e$). The effective mass term $M_0 - M_1 k_z^2$ in Eq. (3), with parameters obtained from experiments, leads to similar Fermi velocities in both systems though Na_3Bi has a larger k_F wave vector than Cd_3As_2.

(vii) As in previous work [11] we measure E_F from $E_0 = 7.6$ meV. This suggests that E_F will locate inside the range of the Berry curvature when the electron density is lower than $N_e \sim 4 \times 10^{18}$ cm^{-3} at low temperatures at which we have $E_F < E_1 - E_0$ meV [33].

For a n-type 3D DSM, the valence band is fully occupied and electronic transitions occur from the valence to the conduction band. The density of states (DOS) for the conduction band is given by

$$D_+(E) = -(g_s/\pi) \sum_{k,k_z} \delta(E - E_{\mathbf{K},+}), \tag{7}$$

where $g_s = 2$ counts for spin degeneracy. Though one of the sums can be evaluated analytically, the result is too cumbersome to be given here. Instead, the δ function is replaced by a Lorentzian, of width $\Gamma = 1$ meV, and the integrals over k and k_z are carried out numerically.

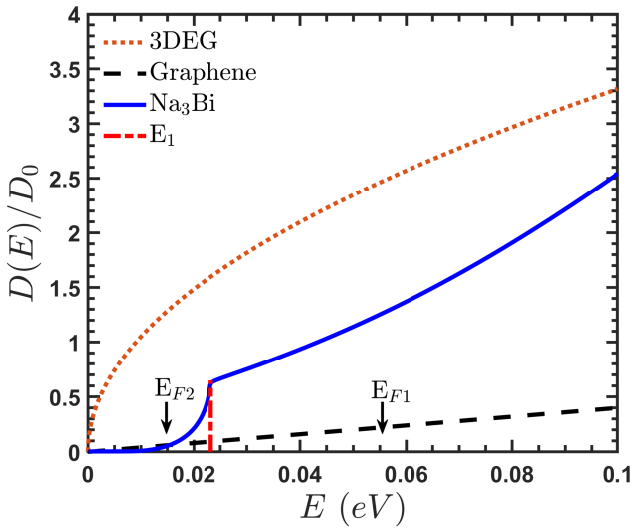

FIG. 2. Density of states (DOS) $D(E)$ for Na_3Bi as a function of the electron energy E (blue curve) with $D_0 = C_0^2/A^3$ for Na_3Bi. The top of the Berry curvature in the conduction band is $E_1 \simeq 23.2$ meV and is marked by the red-dashed curve. At this value of the energy the velocity $\partial E_K/\partial k_z$ vanishes (cf. Fig. 1), i.e., it corresponds to an integrable van Hove singularity. The DOS for a 3DEG is shown by the orange-dotted curve using the effective mass $m^* \simeq 0.11 m_e$ of Na_3Bi and $D_0 = m^{*3/2}\sqrt{2|C_0|}/(\pi\hbar^3)$ for a 3DEG. The black-dashed curve is the result for graphene with energy dispersion $E = \hbar v_F k$ and $D_0 = C_0^2/(\hbar v_F)^3$. Arrows indicate the two values of E_F used to obtain the results shown in Figs. 3 - 6.

In Fig. 2, we show the DOS $D(E)$ as a function of the electron energy E based on Eq. (7). For clarity we contrast it with the result for a 3DEG and that for graphene using the details given in the caption. As is known, for a 3DEG the DOS is $D(E)_{3D} = \sqrt{2m^{*3}E}/(\pi\hbar)^2 \propto E^{1/2}$. The sharp contrast between the two DOSs implies that a 3DEG has different physical properties than 3D DSMs especially for $E < E_1$, i.e., when E_F is relatively low and near the Berry curvature. As can be seen, the effect of the Berry curvature is still clear for energies lower than $E_1 \simeq 23.2$ meV.

These properties of the DOS for 3D DSMs imply that their plasmon modes, for low energies and small momentum, should mainly occur for small q_z. In addition, it's worth pointing out that the variation of the DOS in Cd_3As_2 will be different from that of Na_3Bi although the two systems are similar and have the same energy dispersion. Based on the results of Fig. 1, the electron energy for Cd_3As_2 along different wave vector directions shows much less difference than in Na_3Bi, which means that the DOS in Cd_3As_2 changes less. In addi-

tion, the effect of Berry curvature in Cd_3As_2 will be weaker than in Na_3Bi and will lead to more weakly anisotropic properties in Cd_3As_2; this is in line with the experimental finding in Na_3Bi [4, 5] and Cd_3As_2 [6, 7].

III. DIELECTRIC FUNCTIONS

As we stated in Sec. II, for bulk 3D DSMs the low energy electronic excitations along k and k_z directions are well described by the effective Hamiltonian Eq. (2). Thus, we can study their anisotropic plasmon modes by applying Eqs. (3)-(5) to the RPA dielectric functions based on a 3D Coulomb potential $V(\mathbf{R})$ with $\mathbf{R}=(x,y,z)$.

The electrostatic potential induced by the bare electron-electron (e-e) interaction, $V(\mathbf{R})=e^2/(\kappa|\mathbf{R}|)$, can be calculated via [34]

$$\begin{aligned} V_{ind}(\mathbf{Q},t) &= V_Q \sum_{\mathbf{K}}\sum_{l,l'} \langle \mathbf{K}+\mathbf{Q},l'|\delta N|\mathbf{K},l\rangle\langle \mathbf{K}+\mathbf{Q},l'|e^{-i\mathbf{Q}\cdot\mathbf{R}}|\mathbf{K},l\rangle \\ &= \lim_{\eta\to 0} V_Q V(\mathbf{Q},t)\sum_{\mathbf{K}}\sum_{l,l'} F_{l',l}(\mathbf{K},\mathbf{Q})\Pi_{l',l}(\omega;\mathbf{K},\mathbf{Q}), \end{aligned} \tag{8}$$

where

$$\Pi_{l',l}(\omega;\mathbf{K},\mathbf{Q}) = g_s \frac{f_{l'}(E_{\mathbf{K}+\mathbf{Q},l'})-f_l(E_{\mathbf{K},l})}{E_{\mathbf{K}+\mathbf{Q},l'}-E_{\mathbf{K},l}-\hbar\omega+i\hbar\eta}, \tag{9}$$

is the corresponding density-density correlation function and $f_l(x)=[e^{(x-E_F^l)/k_BT}+1]^{-1}$ is the Fermi-Dirac distribution function. Further, E_F^l is the Fermi energy or chemical potential just above the band l and $g_s=2$ counts for spin degeneracy. Here, the conservation law for momentum flowing into and out of the interaction region has been applied, κ is the dielectric constant for Na_3Bi or Cd_3As_2, $\mathbf{Q}=(\mathbf{q},\varphi,q_z)$ is the change of the electron wave vector during an e-e scattering event, and $V_Q=4\pi e^2/(\kappa Q^2)$ is the 3D Fourier transform of the Coulomb potential induced by the e-e interaction. δN is the induced density and $V(\mathbf{Q},t)$ is the total self-consistent perturbed potential energy.

Using the expressions for the dielectric function $\hat{\mathscr{E}}(\omega,\mathbf{Q})$, induced and total potential energy, we obtain

$$\begin{aligned} \hat{\mathscr{E}}(\omega,\mathbf{Q}) &= 1-\frac{V_{ind}(\mathbf{Q},t)}{V(\mathbf{Q},t)} \\ &= 1-\lim_{\eta\to 0} V_Q \sum_{\mathbf{K}}\sum_{l,l'} F_{l',l}(\mathbf{K},\mathbf{Q})\Pi_{l',l}(\omega;\mathbf{K},\mathbf{Q}), \end{aligned} \tag{10}$$

where $F(\mathbf{K},\mathbf{Q})$ is the form factor for many-body interactions given by

$$\begin{aligned} F_{l',l}(\mathbf{K},\mathbf{Q}) &= |\langle \mathbf{K}+\mathbf{Q},l'|e^{-i\mathbf{Q}\cdot\mathbf{R}}|\mathbf{K},l\rangle|^2 \\ &= |a^*_{\mathbf{K}+\mathbf{Q},l'}a_{\mathbf{K},l}(1+b^*_{\mathbf{K}+\mathbf{Q},l'}b_{\mathbf{K},l})|^2 \\ &= \left| \frac{A^2k|\mathbf{k}+\mathbf{q}|}{\sqrt{(\xi^2_{\mathbf{K}+\mathbf{Q},l'}+A^2|\mathbf{k}+\mathbf{q}|^2)(\xi^2_{\mathbf{K},l}+A^2k^2)}} \right. \\ &\quad \left. \times\left(1+\frac{ll'\xi_{\mathbf{K},l}\xi_{\mathbf{K}+\mathbf{Q},l'}}{A^2[k^2+(k_x-ik_y)(q_x+iq_y)]}\right)\right|^2, \end{aligned} \tag{11}$$

here, $|\mathbf{k}+\mathbf{q}|^2=k^2+q^2+2kq(\cos\theta\cos\varphi+\sin\theta\sin\varphi)=k^2+q^2+2kq\cos(\theta-\varphi)$, θ is the angle between $\mathbf{k}$ and x-axis, and φ is the angle between $\mathbf{q}$ and x-axis. Eventually, the dielectric function takes the form

$$\begin{aligned} \hat{\mathscr{E}}(\omega,\mathbf{Q}) =& 1-\lim_{\eta\to 0}\frac{4\pi e^2 g_s}{\kappa Q^2}\sum_{\mathbf{K}}\sum_{l',l} F_{l',l}(\mathbf{K},\mathbf{Q}) \\ &\times \frac{f_{l'}(E_{\mathbf{K}+\mathbf{Q},l'})-f_l(E_{\mathbf{K},l})}{E_{\mathbf{K}+\mathbf{Q},l'}-E_{\mathbf{K},l}-\hbar\omega-i\hbar\eta}. \end{aligned} \tag{12}$$

We now use the identity: $\lim_{\eta\to 0}[1/(x\pm i\eta)]=\mathscr{P}\{1/x\}\mp i\pi\delta(x)$, with $\mathscr{P}\{1/x\}$ the principal value and $\delta(x)$ the Dirac delta function, to obtain the real and imaginary parts of the dielectric function. Moreover, we replace $\hbar\eta$ by a small value Γ, assumed to be caused, e.g., by impurity scattering. Then, we obtain the real part

$$\begin{aligned} \mathscr{E}_{Re}(\omega,\mathbf{Q}) =& 1-\frac{4\pi e^2 g_s}{\kappa Q^2}\sum_{\mathbf{K}}\sum_{l',l} F_{l',l}(\mathbf{K},\mathbf{Q}) \\ &\times [f_{l'}(E_{\mathbf{K}+\mathbf{Q},l'})-f_l(E_{\mathbf{K},l})] \\ &\times \frac{(E_{\mathbf{K}+\mathbf{Q},l'}-E_{\mathbf{K},l}-\hbar\omega)}{(E_{\mathbf{K}+\mathbf{Q},l'}-E_{\mathbf{K},l}-\hbar\omega)^2+\Gamma^2}. \end{aligned} \tag{13}$$

Meanwhile, the imaginary part $\mathscr{E}_{Im}(\omega,\mathbf{Q})$ becomes

$$\begin{aligned} \mathscr{E}_{Im}(\omega,\mathbf{Q}) =& \frac{4\pi^2 e^2 g_s}{\kappa Q^2}\sum_{\mathbf{K}}\sum_{l',l} F_{l',l}(\mathbf{K},\mathbf{Q})[f_{l'}(E_{\mathbf{K}+\mathbf{Q},l'}) \\ &- f_l(E_{\mathbf{K},l})]\delta(E_{\mathbf{K}+\mathbf{Q},l'}-E_{\mathbf{K},l}-\hbar\omega). \end{aligned} \tag{14}$$

It is very difficult to study the plasmon mode along an arbitrary direction of the 3D wave vector $\mathbf{Q}$. Instead, we decompose it in two components: $\mathbf{Q}_\perp=(0,0,q_z)$ perpendicular to the (x,y) plane, which will only act along the k_z direction, and $\mathbf{Q}_\parallel=(q,\varphi,0)$, with φ the angle between $\mathbf{q}$ and x-axis, which is parallel to this plane.

A. Q perpendicular to the (x,y) plane

In the first case, the real part of $\hat{\mathscr{E}}(\mathbf{K},\mathbf{Q})$ from Eq. (13) for $\mathbf{Q}_\perp=(0,0,q_z)$ becomes

$$\begin{aligned} \mathscr{E}^\perp_{Re}(\omega,q_z) =& 1-\frac{8e^2}{\kappa\pi q_z^2}\sum_{l',l}\int_0^\infty dk_z\int_0^\infty dk k \\ &\times F_{l',l}(\mathbf{K},q_z)[f_{l'}(E_{\mathbf{K},q_z,l'})-f_l(E_{\mathbf{K},l})] \\ &\times \frac{(E_{\mathbf{K},qz,l'}-E_{\mathbf{K},l}-\hbar\omega)}{(E_{\mathbf{K},qz,l'}-E_{\mathbf{K},l}-\hbar\omega)^2+\Gamma^2}, \end{aligned} \tag{15}$$

with

$$E_{\mathbf{K},q_z,l'} = C_0+C_1(k_z+q_z)^2+C_2k^2+l'\sqrt{M^2_{q_z}+A^2k^2}, \tag{16}$$

$$\begin{aligned} M_{q_z} &= [M_0-M_1(k_z+q_z)^2-M_2k^2], \\ F_{l',l}(\mathbf{K},q_z) &= \left|\frac{A^2k^2}{\sqrt{(\xi^2_{\mathbf{K},q_z,l'}+A^2k^2)(\xi^2_{\mathbf{K},l}+A^2k^2)}}\right. \\ &\quad \left.\times\left(1+ll'\xi_{\mathbf{K},l}\xi_{\mathbf{K},q_z,l'}\Big/A^2k^2\right)\right|^2, \end{aligned} \tag{17}$$

where

$$\xi_{\mathbf{K},q_z,l'} = \sqrt{M_{q_z}^2 + A^2k^2} - l'M_{q_z}. \quad (18)$$

In the meantime, assuming a broadening of the energy levels due to scattering we can write $\delta(E) \approx (\Gamma/\pi)(E^2+\Gamma^2)^{-1}$ in Eq. (14), where $\Gamma = \hbar/\tau$ and τ is the lifetime. Then the imaginary part of $\hat{\mathscr{E}}(\mathbf{K},\mathbf{Q})$ for $\mathbf{Q}_\perp = (0,0,q_z)$ becomes

$$\begin{aligned}\mathscr{E}_{Im}^{\perp}(\omega,q_z) =& \frac{8e^2\hbar}{\kappa\pi\tau q_z^2}\sum_{l',l}\int_0^\infty dk_z\int_0^\infty dkk \\ &\times F_{l',l}(\mathbf{K},q_z)[f_{l'}(E_{\mathbf{K},q_z,l'}) - f_l(E_{\mathbf{K},l})] \\ &\times \left[\Gamma^2 + (E_{\mathbf{K},qz,l'} - E_{\mathbf{K},l} - \hbar\omega)^2\right]^{-1}. \quad (19)\end{aligned}$$

B. Q parallel to the (x,y) plane

In this case we take the wavevector $\mathbf{Q}$ as $\mathbf{Q}_\parallel = (q,\varphi,0)$ where φ is the angle between $\mathbf{q}$ and x-axis. From Eq. (13), we obtain the real part of $\hat{\mathscr{E}}(\mathbf{K},\mathbf{Q})$ as

$$\begin{aligned}\mathscr{E}_{Re}^{\parallel}(\omega,\mathbf{q},\varphi) =& 1 - \frac{4e^2}{\kappa\pi^2q^2}\sum_{l',l}\int_0^\infty dk_z\int_0^{2\pi-\varphi} d\phi\int_0^\infty dkk \\ &\times F_{l',l}(\mathbf{K},\mathbf{q},\varphi)[f_{l'}(E_{\mathbf{K},\mathbf{q},\varphi}) - f_l(E_{\mathbf{K}})] \\ &\times \frac{E_{\mathbf{K},\mathbf{q},\varphi} - E_{\mathbf{K}} - \hbar\omega}{(E_{\mathbf{K},\mathbf{q},\varphi} - E_{\mathbf{K}} - \hbar\omega)^2 + \Gamma^2} \quad (20)\end{aligned}$$

with

$$E_{\mathbf{K},\mathbf{q},\varphi} = C_0 + C_1k_z^2 + C_2|\mathbf{k}+\mathbf{q}|^2 + l'\sqrt{M_q^2 + A^2|\mathbf{k}+\mathbf{q}|^2}, \quad (21)$$

where $M_q = M_0 - M_1k_z^2 - M_2|\mathbf{k}+\mathbf{q}|^2$,

$$\begin{aligned}F_{l',l}(\mathbf{K},\mathbf{q},\varphi) =& \left|\frac{A^2k|\mathbf{k}+\mathbf{q}|}{\sqrt{(\xi_{\mathbf{K},\mathbf{q},\varphi,l'}^2 + A^2|\mathbf{k}+\mathbf{q}|^2)(\xi_{\mathbf{K},l}^2 + A^2k^2)}}\right. \\ &\left.\times\left(1 + ll'\xi_{\mathbf{K},l}\xi_{\mathbf{K},\mathbf{q},\varphi,l'}\Big/A^2k|\mathbf{k}+\mathbf{q}|\right)\right|^2, \quad (22)\end{aligned}$$

and

$$\xi_{\mathbf{K},\mathbf{q},\varphi,l'} = \sqrt{M_q^2 + A^2|\mathbf{k}+\mathbf{q}|^2} - l'M_q. \quad (23)$$

By applying relaxation time approximation to Eq. (14), the imaginary part of $\hat{\mathscr{E}}(\mathbf{K},\mathbf{Q})$ for $\mathbf{Q}_\parallel = (\mathbf{q},\varphi,0)$ has the form

$$\begin{aligned}\mathscr{E}_{Im}^{\parallel}(\omega,\mathbf{q},\varphi) =& \frac{4e^2\hbar}{\kappa\pi^2\tau q^2}\sum_{l',l}\int_0^\infty dk_z\int_0^{2\pi-\varphi} d\phi\int_0^\infty dkk \\ &\times F_{l',l}(\mathbf{K},\mathbf{q},\varphi)[f_{l'}(E_{\mathbf{K},\mathbf{q},\varphi}) - f_l(E_{\mathbf{K}})] \\ &\times \left[\Gamma^2 + (E_{\mathbf{K},\mathbf{q},\varphi,l'} - E_{\mathbf{K},l} - \hbar\omega)^2\right]^{-1}. \quad (24)\end{aligned}$$

Here, we made the change $\phi = \theta - \varphi$, so that $|\mathbf{k}+\mathbf{q}|^2 = k^2 + q^2 + 2kq\cos(\theta-\varphi)$. Then the integration over θ from 0 to 2π becomes one over ϕ from 0 to $(2\pi-\varphi)$, which describes how different wave vector $\mathbf{q}$ directions affect the dielectric function. After obtaining the expressions of the dielectric function for 3D DSMs in different directions, we consider the transitions between different energy bands. The band index $l = 1$ (-1) represents the conduction (valence) band, and the dielectric function will have four parts

$$\sum_{ll'}\hat{\mathscr{E}} = \mathscr{E}_{++} + \mathscr{E}_{-+} + \mathscr{E}_{+-} + \mathscr{E}_{--}. \quad (25)$$

Since we focus on n-type 3D DSMs, in which the conduction band is occupied, the valence band is fully occupied so that $f_-(x) = 1$, and $\Pi_{l',l}(\omega;\mathbf{K},\mathbf{Q}) = 0$ for $l' = l = -1$. At the same time, electron transitions from the conduction band $(l=+1)$ to the valence band $(l'=-1)$ have only a very small influence on plasmon modes, so we take $\mathscr{E}_{+-} \simeq 0$. Thus, eventually we consider only intraband transitions in the conduction band $(\mathscr{E}_{++})$ and interband transitions from the valence to the conduction band $(\mathscr{E}_{-+})$ into account. Then, the resulting plasmon modes are the solutions of $Re[\hat{\mathscr{E}}(\omega,\mathbf{Q})] = |\mathscr{E}_{Re}(\omega,\mathbf{Q})| = 0$. The energy loss rate can be evaluated using the imaginary part of the dielectric function through the energy loss function:

$$E_{loss} = -Im\left[\frac{1}{\hat{\mathscr{E}}(\omega,\mathbf{Q})}\right] = \frac{-\mathscr{E}_{Im}(\omega,\mathbf{Q})}{\mathscr{E}_{Re}(\omega,\mathbf{Q})^2 - \mathscr{E}_{Im}(\omega,\mathbf{Q})^2}. \quad (26)$$

As shown in Fig. 1, 3D DSMs have anisotropic energy dispersions but in the (x,y) plane their dispersions are isotropic and similar to that of graphene. Thus, we first consider the simple case in which $\mathbf{q}$ is parallel to $\mathbf{k}$ by setting $\varphi = 0$ in Eqs. (20) and (24). Following the standard procedure [40] we first obtain the plasmon dispersion from the zeros of the real part of the dielectric function and then we calculate the energy loss using Eq. (26).

IV. RESULTS AND DISCUSSION

For the numerical calculations we use the band parameters for Na_3Bi shown in Table I [2]. They were determined by fitting the energy spectrum of the effective Hamiltonian in Eq. (1) to those obtained from *ab initio* calculations and the ARPES experimental results [4, 5] since both agree well with those of Ref. [2]. For the 3D DSM Cd_3As_2, the experimental works from ARPES measurements [6, 7] and scanning tunnelling microscopy measurements [29] indicate that the energy spectrum deduced from experiments is basically the same as the theoretical one [3], though with some minor differences. The main one is that the experimentally determined Fermi velocities in Cd_3As_2 [6, 29] are much larger than the theoretical ones [3]. As a result, we use the band parameters from ARPES measurements shown in Table I [29]. Furthermore, it has been shown experimentally that for 3D DSMs, the lifetime is different for samples with different carrier densities, but for low temperatures both Na_3Bi and Cd_3As_2 samples exhibit fast lifetimes ($\sim 1-7$ ps) [10, 35, 36]. Hence, we use 6.71 ps for Na_3Bi [10] and 6.87 ps for Cd_3As_2 [36].

As shown in Fig. 2, the DOSs for 3DEG, graphene, and 3D DSMs are different from each other. Accordingly, their

TABLE I. The energy band parameters and dielectric constant of Na_3Bi are taken from Ref. [2] and Ref. [37], respectively. Note that for Cd_3As_2, the original band parameters are $M_0' = -0.060$ eV, $M_1' = 96$ eVÅ^2, and $M_3 = 0.05$ eV. For small momenta $|k_z| \ll M_3/\sqrt{M_1'}$, the energy dispersion in Cd_3As_2 will have the same form as in Na_3Bi, and the band parameters become: $M_0 = M_0' + |M_3|$ and $M_1 = 0.5M_1'/|M_3|$ in Eqs. (1) - (4) [29]. The dielectric constant for Cd_3As_2 is taken from Ref. [24].

Na_3Bi band parameters			
C_0 (eV)	C_1 (eVÅ^2)	C_2 (eVÅ^2)	M_0 (eV)
-0.06382	8.7536	-8.4008	-0.8686
M_1 (eVÅ^2)	M_2 (eVÅ^2)	A (eVÅ)	κ
-10.6424	-10.361	2.4598	5.99
Cd_3As_2 band parameters			
C_0 (eV)	C_1 (eVÅ^2)	C_2 (eVÅ^2)	M_0 (eV)
-0.219	-30	-16	-0.01
M_1 (eVÅ^2)	M_2 (eVÅ^2)	A (eVÅ)	κ
960	18	2.75	12

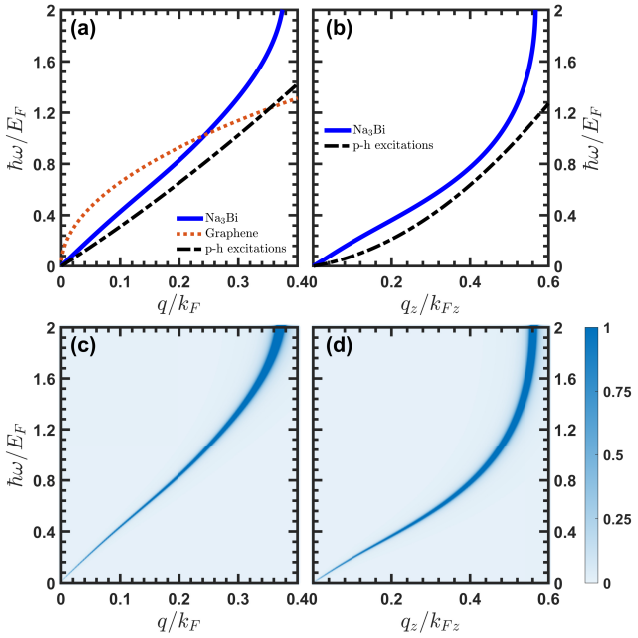

FIG. 3. Dispersion relations and energy loss functions in Na_3Bi along different $\mathbf{Q}$ directions at temperature $T = 10$ K, electron density $N_e = 1\times10^{19}$ cm^{-3} (see green-dashed lines in Fig. 1 (b) and (c), corresponding to $E_{F1} \simeq 59.076$ meV), and lifetime $\tau = 6.71$ ps. In panels (a) and (c) we have $Q_\parallel = (q,\varphi,0)$ at $\varphi = 0$, the Fermi wave vector k_F along the k direction is about $\sim 2.25\times10^8$ m^{-1}. In panels (b) and (d) we have $Q_\perp = (0,0,q_z)$, the Fermi wave vector k_{Fz} along the k_z direction is about $\sim 10.4\times10^8$ m^{-1}. The orange-dotted curve in (a) is graphene's plasmon dispersion relation for $N_e = 1\times10^{12}$ cm^{-2}. The black-dash-dotted curves in (a) and (b) represent, for a 3DEG with $m^* \simeq 0.24m_e$, the beginning of the particle-hole (p-h) excitations area in which $\omega \simeq \hbar^2(q^2+2qk_F)/2m^*$.

plasmon modes will also be different. In the long-wavelength limit ($\mathbf{Q}\to0$), the plasmon dispersion of 3DEG is given by an optical-like formula $\omega_Q = \omega_P + 3v_F^2Q^2/(10\omega_P) \sim Q^2$, where $\omega_P = [N_e e^2/(m\kappa_0)]^{1/2}$ is the plasma frequency, κ_0 the vacuum dielectric constant, and $v_F = \hbar k_F/m$ is the Fermi velocity. In a real metal, e.g., sodium, we have $N_e \sim 10^{23}$ cm^{-3}, the plasmon energy $\hbar\omega_P \sim 5.9$ eV is much larger than $k_BT \sim 25$ meV, so that plasmons in a 3DEG are not easily, i.e., thermally excitable; this means it's very difficult to directly observe them in experiments. However, for graphene in the long-wavelength limit ($\mathbf{q}\to0$), the dispersion relation $\omega_q = (2e^2E_Fq/\kappa_0)^{1/2} \sim q^{1/2} \sim N_e^{1/4}$ with $E_F = \hbar v_F k_F$, $k_F = (\pi N_e)^{1/2}$, is acoustic-like and depends strongly on q [38]. In addition, a conventional 2D electron gas (2DEG) has a dispersion relation similar to graphene $\omega_q \sim q^{1/2} \sim N_e^{1/2}$ [39]. The plasmon energies for both 2DEG and graphene are $\hbar\omega_q \to 0$ for $q\to0$, i.e., quite small. Consequently, plasmons in them are easier to excite and observe in experiments.

Fig. 3 shows the plasmon dispersion and energy loss rate for different wave vector directions for high electron density in Na_3Bi and fixed temperature. The corresponding Fermi level is much higher than the Berry curvature (cf. green-dashed line in Fig. 1 (b) and (c)), and the Fermi wave vector k_{Fz} is about five times larger than k_F.

We notice the following features.

(i) Panels (a) and (b) in Fig. 3 show the dispersion relations along q and q_z are anisotropic in Na_3Bi. This is in line with the anisotropic band structure of Na_3Bi shown in Fig. 1 (b) and (c) which indicates that its electron excitation energy $E_\mathbf{K}$ requires a different momentum k or k_z along different directions.

(ii) The plasmon energy $\hbar\omega\to0$, in the long-wavelength limit $q\to0$ and $q_z\to0$, which is in sharp contrast with the results for a 3DEG and also with those for 3D DSMs with a single Dirac point [24–26]. The collective oscillations of electrons should be easier to excite and observe in Na_3Bi due to its unique energy band.

(iii) The dispersions are linear for small q or q_z ($\hbar\omega \propto q$, q_z), but with increasing q or q_z, they become similar to that of a 3DEG ($\hbar\omega \propto q^2$ or q_z^2). Also, these changes are more distinct vs q_z in Fig. 3 (b) and (d) than vs q in Fig. 3 (a) and (c). In Fig. 1 (b) we found that the electron energy along the k direction is approximately linear in k in a higher energy range, but along the k_z direction, cf. Fig. 1 (c), it is linear only close to the Dirac points whereas at high energies it becomes parabolic. That is, the plasmon dispersion vs q is linear in a broader range than vs q_z.

(iv) The energy loss function, corresponding to panels (a) and (b), is shown in panels (c) and (d), respectively. As expected, plasmons appear as peaks in the energy loss functions for both $Q_\parallel$ and $Q_\perp$. Meanwhile, the wave vector dependence is consistent with that of the plasmon dispersion and it is anisotropic. The energy loss peaks are broader at large q and q_z, but still they converge up to a high energy $\hbar\omega = 2E_F$.

(v) The plasmon energies will involve the particle-hole (p-h) excitation continuum in 3DEG, graphene [39], and single-cone 3D DSMs [25, 26], e.g, for $\hbar\omega < \hbar^2(Q_c^2 + 2Q_cK_F)/(2m^*)$ and $Q > Q_c$ in 3DEG. However, we found that

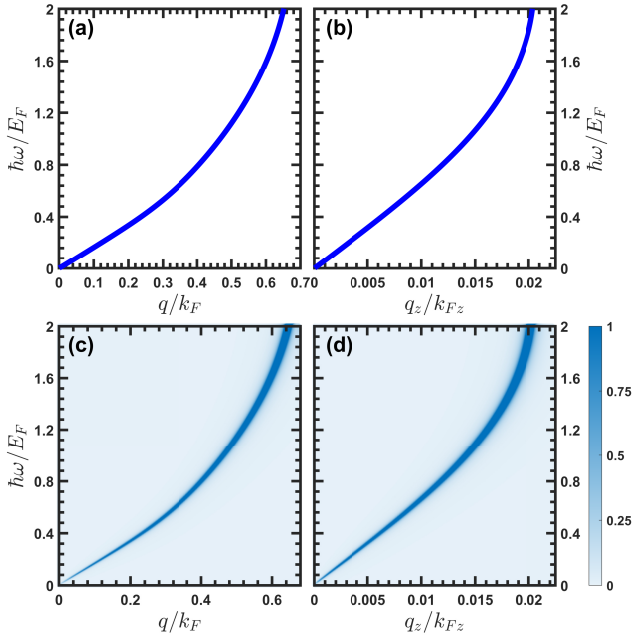

FIG. 4. As in Fig. 3 with electron density $N_e = 1\times10^{17}$ cm^{-3} (see black-dotted lines in Fig. 1 (b) and (c), corresponding to $E_{F2} \simeq 14.634$ meV). For $Q_\parallel = (\mathrm{q},\varphi,0)$ at $\varphi = 0$, the Fermi wave vector k_F along the k direction is about $\sim 0.298\times10^8$ m^{-1}. For $Q_\perp = (0,0,q_z)$, the Fermi wave-vector k_{Fz} along the k_z axis is about $\sim 9.24\times10^8$ m^{-1}.

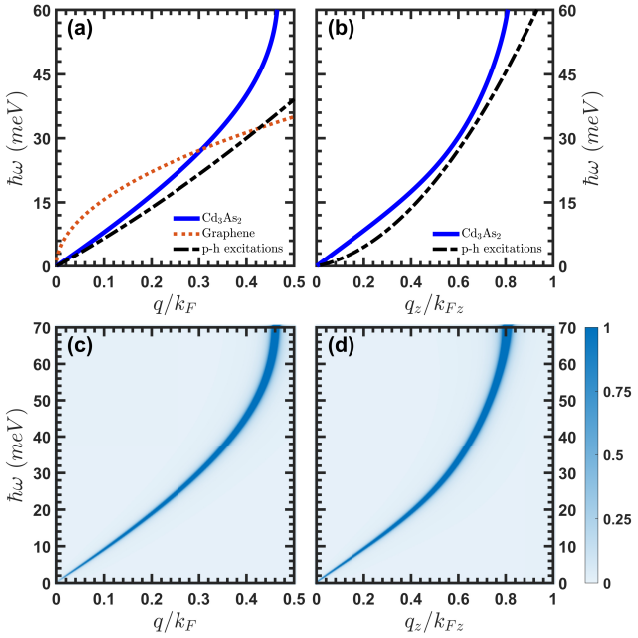

FIG. 5. Plasmon dispersions and energy loss functions in Cd_3As_2 along different $\mathbf{Q}$ directions at fixed temperature $T = 10$ K, electron density $N_e = 1\times10^{19}$ cm^{-3} (see Fig. 1 (e) and (f), corresponding to $E_{F1} \simeq -185.651$ meV), and lifetime $\tau = 6.87$ ps. For $Q_\parallel = (\mathrm{q},\varphi,0)$ at $\varphi = 0$, the Fermi wave vector k_F along the k direction is about $\sim 1.33\times10^8$ m^{-1}. For $Q_\perp = (0,0,q_z)$, the Fermi wave vector k_{Fz} along the k_z axis is about $\sim 0.68\times10^8$ m^{-1}. The orange-dotted curve in (a) is graphene's dispersion relation for $N_e = 1\times10^{12}$ cm^{-2}. The black-dash-dotted curves in (a) and (b) represent, for a 3DEG with $m^* \simeq 0.24m_e$, the beginning of the particle-hole (p-h) excitations area in which $\omega \simeq \hbar^2(q^2+2qk_F)/2m^*$.

in Na_3Bi the plasmon dispersion curves only occur in a relatively small wave vector range and the plasmon energies are above the continuum of the 3D p-h excitations in the entire wave vector range in both Fig. 3 (a) and (b). Meanwhile, we would like to point out that this work is based on the effective Hamiltonian, which is only valid for small momenta and low-energy ranges. Thus, our study indicates that plasmons in Na_3Bi do not merge into the Landau damping range, i.e., the plasmon energy will not decay by single-particle excitations for small q and q_z.

The results of Fig. 3 are for high values of the electron density $N_e = 1\times10^{19}$ cm^{-3} and E_F is much higher than the energy for Berry curvature region, cf. green-dashed line in Fig. 1 (b). A significant change occurs for low electron density, $N_e = 1\times10^{17}$ cm^{-3} and E_F is lower than the Berry curvature, cf. black-dotted line in Fig. 1 (b). The results are shown in Fig. 4. Although the overall trend looks similar, the range of the relevant wave vectors changes. In particular, that for q_z shrinks dramatically, it's approximately 30 times shorter whereas q is only about 4 times shorter. This due to the presence of the Berry curvature in energy bands. As seen from Fig. 2, the DOS of Na_3Bi decreases rapidly with decreasing E_F, especially for $E_F < E_1$, and Fig. 1 indicates that the Berry curvature mainly effects the energy along k_z direction. As a result, reducing electron doping leads to a much smaller wave vector dependence of plasmon dispersion for $Q_\perp$. Similar effects of the Berry curvature were reported in Ref. [11].

The results shown in Figs. 3 and 4 are for Na_3Bi. The corresponding ones for Cd_3As_2 are shown in Figs. 5 and 6, respectively. As shown, the plasmon dispersion relations and energy losses for high electron density Cd_3As_2 are similar to those in Na_3Bi. In some detail we observe the following.

(i) The plasmon energies are $\hbar\omega \to 0$ for $q \to 0$ and $q_z \to 0$.

(ii) The plasmon modes are anisotropic, the plasmon dispersions are linear for small q and q_z but become parabolic with increasing q and q_z. The dispersion for q is linear in a boarder range than q_z.

(iii) The plasmon energies in both directions do not involve p-h excitations so its plasma oscillations will also not be damped nor will they decay into the single-particle continuum. For low electron densities, cf. Fig. 6, a significant small q_z dependence for plasmon energy can be found and results from the Berry curvature of the energy band.

The overall trend is similar to Na_3Bi, but we notice some differences between Na_3Bi and Cd_3As_2. We mentioned that Cd_3As_2 has less anisotropic properties than Na_3Bi in Figs. 1 and 2. Specifically, when we reduce the electron doping, both plasmon wave vectors for Na_3Bi and Cd_3As_2 will decrease, but the q_z range in Na_3Bi will shrink much more than that in Cd_3As_2 . In addition, the k_{Fz} value in Cd_3As_2 is smaller than its k_F whereas in Na_3Bi k_{Fz} is about 20 times larger than its k_F. We emphasize that in both 3D DSMs the distance of E_F from the Berry curvature importantly affects the pertinent

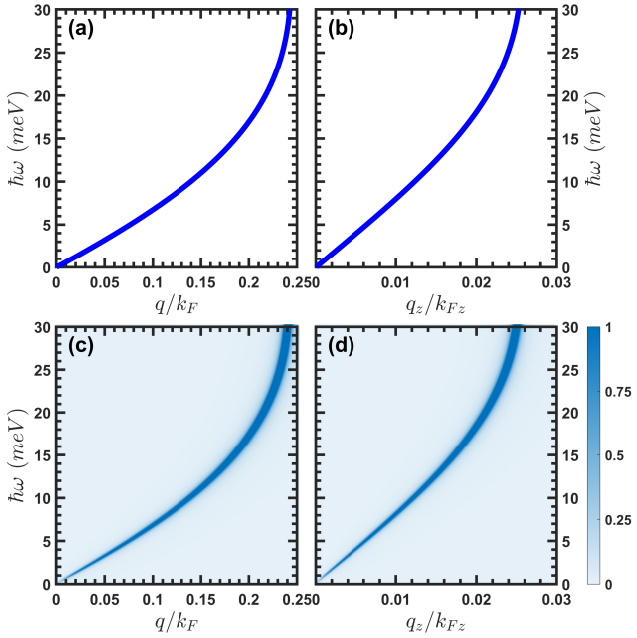

FIG. 6. As in Fig. 5 with electron density $N_e = 1\times10^{17}$ cm^{-3} (see Fig. 1 (e) and (f), corresponding to $E_{F2} \simeq -211.237$ meV). For $Q_{\parallel} = (\mathbf{q}, \varphi, 0)$ at $\varphi = 0$, the Fermi wave vector k_F along the k direction is about $\sim 0.301\times10^8$ m^{-1}). For $Q_{\perp} = (0,0,q_z)$, the Fermi wave-vector k_{Fz} along the k_z axis is about $\sim 0.438\times10^8$ m^{-1}.

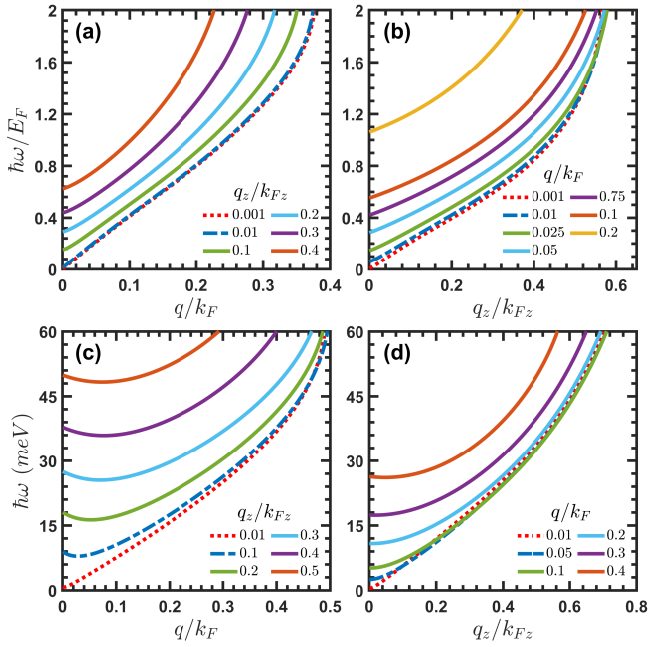

FIG. 7. (a) Plasmon dispersion for Na_3Bi as a function of q at fixed temperature $T = 10$ K, electron density $N_e = 1\times10^{19}$ cm^{-3}, lifetime $\tau = 6.71$ ps, and fixed q_z. (b) Plasmon dispersion for Na_3Bi with q and q_z interchanged is shown. (c), (d): *idem.* as in (a) and (b), respectively, for Cd_3As_2 for the same temperature and electron density, and $\tau = 6.87$ ps. All curves for selected q_z or q isovalues are marked as shown in the insets.

wave vector ranges.

Finally, it is of interest to see how the results vs q change when q_z is not zero and how the results change vs q_z when q takes certain values. We show them in Fig. 7 for Na_3Bi on panels (a) and (b) and for Cd_3As_2 in panels (c) and (d), using the parameters of the caption and the constant q_z or q values specified in the insets. As shown in Fig. 7, for $q_z \neq 0$ (or $q \neq 0$) the dispersion becomes similar to that of a 3DEG as either q_z or q take some constant values and the anisotropic features are distinct.

Considering the results from all figures, we see that the plasmon modes in the bulk materials Na_3Bi and Cd_3As_2, show unique properties and advantages over other materials. For instance, 3D DSMs have similar gapless Dirac properties as graphene, such as high carrier mobility, but the samples for bulk 3D DSMs are easier to manufacture. Also, in 3D DSMs the plasmons are easier to observe than in metals due to the their energy $\hbar\omega$ being close to $k_BT \sim 25$ meV as we discussed before. The Fermi energy E_F related to the carrier density is gate-tunable in 3D DSMs [12], therefor the plasmons, which are sensitively affected by the position of E_F relative to the Berry curvature region of the bands, will also have the anisotropic gate-tunable properties in sharp contrast to other 3D materials such as multilayered graphene [27], Weyl semimetals [28], and isotropic Dirac semimetals [26]. Furthermore, other interesting properties, such as anisotropic plasmon polaritons and surface plasmons can be expected based on our results.

V. SUMMARY

We presented a premiere RPA treatment of collective excitations in the three-dimensional (3D) Dirac semimetals (DSMs) Na_3Bi and Cd_3As_2 using one-electron properties derived from a $\mathbf{k}\cdot\mathbf{p}$ Hamiltonian. The density of states of these Dirac semimetals differ significantly from those of a 3D electron gas or graphene. The anisotropy of the one-electron spectrum shows up in the dispersion relations that are markedly different from those of graphene or a 3D electron gas. The same holds for the energy-loss function. There are important differences between results valid for high and low electron densities that result in the Fermi energy being far or close to the region of the Berry curvature of the bands. A one particularly worth mentioning is that for E_F less than the energy at which v_z vanishes, the range of the relevant wave vectors q and q_z shrinks, especially the one for q_z shrinks by nearly a factor of 10. Therefore, changing the electron density of 3D Dirac semimetals will allow one to tune the frequency range of their plasmon modes, particularly along the z-direction. Moreover, other intriguing properties like anisotropic plasmon polaritons and surface plasmons, which will also be affected by electron density due to the Berry curvature of the energy band, can be expected.

ACKNOWLEDGEMENTS

Q. N. Li acknowledges financial support from China Scholarship Council (No. 202207030017). This work was also supported by the National Natural Science foundation of China (Grants No. U2230122, No. U2067207, and No. 12364009), the Research Foundation Flanders (FWO-Vl), and Shenzhen Science and Technology Program (Grant No. KQTD20190929173954826).

[1] S. M. Young, S. Zaheer, J. C. Y. Teo, C. L. Kane, E. J. Mele, and A. M. Rappe, Phys. Rev. Lett. **108**, 140405 (2012).

[2] Z. J. Wang, Y. Sun, X. Q. Chen, C. Franchini, G. Xu, H. M. Weng, X. Dai, and Z. Fang, Phys. Rev. B **85**, 195320 (2012).

[3] Z. J. Wang, H. M. Weng, Q. S. Wu, X. Dai, and Z. Fang Phys. Rev. B **88**, 125427 (2013).

[4] S.-Y. Xu, C. Liu, S. K. Kushwaha, R. Sankar, J. W. Krizan, I. Belopolski, M. Neupane, G. Bian, N. Alidoust, T.-R. Chang, H.-T. Jeng, C.-Y. Huang, W.-F. Tsai, H. Lin, P. P. Shibayev, F.-C. Chou, R. J. Cava, and M. Z. Hasan, Science **347**, 294 (2014).

[5] Z. K. Liu, B. Zhou, Y. Zhang, Z. J. Wang, H. M. Weng, D. Prabhakaran, S.-K.Mo, Z. X. Shen, Z. Fang, X. Dai, Z. Hussain, and Y. L. Chen, Science **343**, 864 (2014).

[6] M. Neupane, S.-Y. Xu, R. Sankar, N. Alidoust, G. Bian, C. Liu, I. Belopolski, T.-R. Chang, H.-T. Jeng, H. Lin, A. Bansil, F. C. Chou, and M. Z. Hasan, Nat Commun **5**, 3786 (2014).

[7] Z. K. Liu, J. Jiang, Zhou, B, B. Zhou, Z. J. Wang, Y. Zhang, H. M. Weng, D. Prabhakaran, S-K. Mo, H. Peng, P. Dudin, T. Kim, M. Hoesch, Z. Fang, X. Dai, Z. X. Shen, D. L. Feng, Z. Hussain, and Y. L. Chen, Nature Mater **13**, 677 (2014).

[8] S. Borisenko, Q. Gibson, D. Evtushinsky, V. Zabolotnyy, B. Büchner, and R. J. Cava, Phys. Rev. Lett. **113**, 027603 (2014).

[9] T. Liang, Q. Gibson, M. N. Ali, M. Liu, R. J. Cava, and N. P. Ong, Nature Mater **14**, 280 (2015).

[10] J. Xiong, S. Kushwaha, J. Krizan, T. Liang, R. J. Cava, and N. P. Ong, Europhys. Lett. 114, 27002 (2016).

[11] H. F. Yuan, W. Xu, X. N. Zhao, D. Song, G. R. Zhang, Y. M. Xiao, L. Ding, and F. M. Peeters, Phys. Rev. B **99**, 235303 (2019).

[12] C.-Z. Li, L.-X. Wang, H. W. Liu, J. Wang, Z.-M. Liao, and D.-P. Yu, Nat Comm **6**, 10137 (2015).

[13] J. Xiong, S. K. Kushwaha, T. Liang, J. W. Krizan, M. Hirschberger, W. D. Wang, R. J. Cava, N. P. Ong, Science **350**, 413 (2015).

[14] S. Zhang, Q. Wu, L. Schoop, M. N. Ali, Y. Shi, N. Ni, Q. Gibson, S. Jiang, V. Sidorov, W. Yi, J. Guo, Y. Zhou, D. Wu, P. Gao, D. Gu, C. Zhang, S. Jiang, K. Yang, A. Li, Y. Li, X. Li, J. Liu, X. Dai, Z. Fang, R. J. Cava, L. Sun, and Z. Zhao, Phys. Rev. B **91**, 165133 (2015).

[15] A. C. Lygo, B. H. Guo, A. Rashidi, V. Huang, P. Cuadros-Romero, and S. Stemmer, Phys. Rev. Lett. **130**, 046201 (2023).

[16] W. Lu, S. F. Ge, X. F. Liu, H. Lu, C. Z. Li, J. W. Lai, C. Zhao, Z. M. Liao, S. Jia, and D. Sun Phys. Rev. B **95**, 024303 (2017).

[17] M. Uchida, Y. Nakazawa, S. Nishihaya, K. Akiba, M. Kriener, Y. Kozuka, A. Miyake, Y. Taguchi, M. Tokunaga, N. Nagaosa, Y. Tokura, and M. Kawasaki, Nat Commun **8**, 2274 (2017).

[18] C. Zhang, Y. Zhang, X. Yuan, S. H. Lu, J. L. Zhang, A. Narayan, Y. W. Liu, H. Q. Zhang, Z. L. Ni, R. Liu, E. S. Choi, A. Suslov, S. Sanvito, L. Pi, H.-Z. Lu, A. C. Potter, and F. X. Xiu, Nature **565**, 331 (2019).

[19] D. Neubauer, J. P. Carbotte, A. A. Nateprov, A. Lohle, M. Dressel, and A. V. Pronin, Phys. Rev. B **93**, 121202(R) (2016).

[20] L. Hou, Y. K. Yang, A. L. Li, Q. J. Wang, Q. N. Li, M. Wu, P. C. Ji, Y. J. Zhang, Y. M. Xiao, W. Xu, F. X. Xiu, and L. Ding Phys. Rev. B **108**, 115416 (2023).

[21] N. P. Armitage, E. J. Mele, and AA. Vishwanath, Rev. Mod. Phys. **90**, 015001 (2018).

[22] A.-Q. Wang, X.-G. Ye, D.-P. Yu, and Z.-M. Liao, ACS Nano **14**, 4, 3755 (2020).

[23] G. S. Jenkins, C. Lane, B. Barbiellini, A. B. Sushkov, R. L. Carey, Fengguang Liu, J. W. Krizan, S. K. Kushwaha, Q. Gibson, Tay-Rong Chang, Horng-Tay Jeng, Hsin Lin, R. J. Cava, A. Bansil, and H. D. Drew, ACS Nano **14**, 4, 3755 (2020).

[24] O. V. Kotov and Yu. E. Lozovik, Phys. Rev. B **93**, 235417 (2016).

[25] A. Thakur, R. Sachdeva, and A. Agarwal, J. Phys.: Condens. Matter **29**, 105701 (2017).

[26] A. Politano, G. Chiarello, B. Ghosh, K. Sadhukhan, C.-N. Kuo, C. S. Lue, V. Pellegrini, and A. Agarwal, Phys. Rev. Lett. **121**, 086804 (2018).

[27] J.-J. Zhu, S. M. Badalyan, and F. M. Peeters, Phys. Rev. B **87**, 085401 (2013).

[28] J. H. Zhou, H.-R. Chang, and D. Xiao, Phys. Rev. B **91**, 035114 (2015).

[29] S. Jeon, B. B. Zhou, A. Gyenis, B. E. Feldman, I. Kimchi, A. C. Potter, Q. D. Gibson, R. J. Cava, A. Vishwanath, and A. Yazdani, Nature Mater **13**, 851 (2014).

[30] J. Z. Cao, S. H. Liang, C. Zhang, Y. W. Liu, J. W. Huang, Z. Jin, Z.-G. Chen, Z. J. Wang, Q. S. Wang, J. Zhao, S. Y. Li, X. Dai, J. Zou, Z. C. Xia, L. Li, and F. X. Xiu, Nat Commun **6**, 7779 (2015).

[31] B. Zhou, H.-Z. Lu, R.-L. Chu, S.-Q. Shen, and Q. Niu, Phys. Rev. Lett. **101**, 246807 (2008).

[32] A. Narayanan, M. D. Watson, S. F. Blake, N. Bruyant, L. Drigo, Y. L. Chen, D. Prabhakaran, B. Yan, C. Felser, T. Kong, P. C. Canfield, and A. I. Coldea, Phys. Rev. Lett. **114**, 117201 (2015).

[33] Q. N. Li, W. Xu, Y. M. Xiao, L. Ding, B. Van Duppen, and F. M. Peeters, J. Appl. Phys. **128**, 155707 (2020).

[34] M. Dressel, G. Gruener, G. F. Bertsch, Am. J. Phys. 70, 1269 (2002).

[35] W. Lu, S. F. Ge, X. F. Liu, H. Lu, C. Z. Li, J. W. Lai, C. Zhao, Z. M. Liao, S. Jia, and D. Sun, Phys. Rev. B **95**, 024303 (2017).

[36] Q. S. Wang, C.-Z. Li, S.F. Ge, J.-G. Li, W. Lu, J. W. Lai, X. F. Liu, J. C. Ma, D.-P. Yu, Z.-M. Liao, and D. Sun, Nano Lett. **17**, 2, 834 (2017).

[37] M. Dadsetani and A. Ebrahimian, J. Electron. Mater. **45**, 5867 (2016).

[38] X.-F. Wang and T. Chakraborty, Phys. Rev. B **75**, 033408 (2007).

[39] H. M. Dong, L. L. Li, W. Y. Wang, S. H. Zhang, C. X. Zhao, W. Xu, Physica E **44**, 9, 1889-1893 (2012).

[40] B. Wunsch, T. Stauber, F. Sols, and F. Guinea, New J. Phys. **8**, 318 (2006).